# Testing the Core/Shell Model of Nanoconfined Water in Reverse Micelles Using Linear and Nonlinear IR Spectroscopy

**Ivan R. Piletic, David E. Moilanen, D. B. Spry, Nancy E. Levinger,[†] and M. D. Fayer***

*Department of Chemistry, Stanford University, Stanford, California 94305*

*Received: February 19, 2006; In Final Form: March 11, 2006*

A core/shell model has often been used to describe water confined to the interior of reverse micelles. The validity of this model for water encapsulated in AOT/isooctane reverse micelles ranging in diameter from 1.7 to 28 nm ($w_0 = 2$–60) and bulk water is investigated using four experimental observables: the hydroxyl stretch absorption spectra, vibrational population relaxation times, orientational relaxation rates, and spectral diffusion dynamics. The time dependent observables are measured with ultrafast infrared spectrally resolved pump–probe and vibrational echo spectroscopies. Major progressive changes appear in all observables as the system moves from bulk water to the smallest water nanopool, $w_0 = 2$. The dynamics are readily distinguishable for reverse micelle sizes smaller than 7 nm in diameter ($w_0 = 20$) compared to the response of bulk water. The results also demonstrate that the size dependent absorption spectra and population relaxation times can be quantitatively predicted using a core–shell model in which the properties of the core (interior of the nanopool) are taken to be those of bulk water and the properties of the shell (water associated with the headgroups) are taken to be those of $w_0 = 2$. A weighted sum of the core and shell components reproduces the size dependent spectra and the nonexponential population relaxation dynamics. However, the same model does not reproduce the spectral diffusion and the orientational relaxation experiments. It is proposed that, when hydrogen bond structural rearrangement is involved (orientational relaxation and spectral diffusion), dynamical coupling between the shell and the core cause the water nanopool to display more homogeneous dynamics. Therefore, the absorption spectra and vibrational lifetime decays can discern different hydrogen bonding environments whereas orientational and spectral diffusion correlation functions predict that the dynamics are size dependent but not as strongly spatially dependent within a reverse micelle.

## I. Introduction

Water has unique properties that are intimately related to its molecular level structure. Water's properties are strongly influenced by its dynamic hydrogen bond network. The hydrogen bond network and, therefore, the properties of water are sensitive to structural and chemical perturbations. An interface with another phase,[1,2] solutes ranging from ions to large biological molecules,[3,4] pH,[5] temperature and pressure[6,7] or any combination of these impacts the hydrogen bond network structure and dynamics. The modification of hydrogen bond dynamics from their bulk characteristics has important ramifications for protein folding, charge-transfer reactions, and reactions that occur at interfaces or in confined environments. A body of experimental and theoretical work has examined the dynamics of water in a variety of environments, for example, water around large biological molecules,[8] around micelles,[9] in reverse micelles,[10–14] in cyclodextrins,[15] and zeolites.[16] The modified dynamics of water in complex chemical and biological systems probed by dielectric relaxation and solvation dynamics experiments have been reviewed recently.[4]

Recent theories[17] and molecular dynamic simulations[18–20] indicate that at least two types of water molecules are present in complex systems, free and bound. Free suggests water molecules with essentially bulk characteristics separated from the interface in the core of the system. Bound water molecules are associated with particular groups in proteins, the interface in reverse micelles, etc. and can reside in pockets separated from the bulk water phase. The long time components observed in dielectric relaxation and solvation dynamics experiments have been attributed to exchange between the associated and core populations.[4]

To properly account for the behavior of water in complex systems requires consideration of the complexity of water itself. Bulk water contains many different hydrogen bonding environments determined by the strength and number of local hydrogen bonds.[21] There are faster and slower relaxation time scales that reflect inertial and diffusive dynamics.[22,23] The presence of a solute or interface will modify the hydrogen bond network and new interactions and environments need to be accounted for. As a result, the response of water in complex systems is expected to exhibit even more complexity than bulk water.

Reverse micelles are small molecular assemblies that encapsulate nanoscopic pools of water. The anionic surfactant aerosol-OT (AOT with $Na^+$ counterion) is known to form spherical reverse micelles in a variety of nonpolar phases. The size of the reverse micelles is readily tuneable by adjusting the $w_0$ value.

$$w_0 = \frac{[H_2O]}{[AOT]} \tag{1}$$

Varying the $w_0$ value allows the dynamics of the nanoscopically confined water to be explored as a function of the water nanopool size. Deviations from bulk behavior can be observed and the size at which bulk-like characteristics appear for a

* Corresponding author. E-mail: fayer@stanford.edu.
† Permanent address: Department of Chemistry, Colorado State University, Fort Collins, CO 80523-1872.

particular observable can be determined. The size for the onset of bulk properties is an important question that has been addressed by several groups although different techniques yield different results.[24]

Ultrafast infrared (IR) vibrational spectroscopy[25] is ideally suited to probe the dynamics of water in reverse micelles. Time dependent vibrational measurements on the hydroxyl stretch of water can resolve different dynamical time scales and relate the dynamics to hydrogen bond network structural evolution. In addition to linear IR absorption spectroscopy, two ultrafast vibrational methods are employed to explicate the dynamics of nanoscopic pools of water in reverse micelles, and the results are compared to those for bulk water. Spectrally resolved pump−probe experiments are used to determine the vibrational population relaxation and the orientational relaxation of the OD stretch of HOD in $H_2O$ as a function of reverse micelle size. Spectrally resolved stimulated vibrational echo spectroscopy[26] measures the different contributions to the spectroscopic line shape and thus the underlying system dynamics through spectral diffusion.

The utility of ultrafast vibrational spectroscopy[25] in probing the dynamics of water arises from the intimate connection between the hydrogen bond network and the water hydroxyl stretch. Hydrogen bonding affects the frequency of the hydroxyl stretch significantly, causing the hydroxyl stretch absorption frequency to red shift, as well as the integrated intensity and the spectral width of the hydroxyl band to increase.[27] The broad hydroxyl stretch absorption arises from a broad distribution of hydrogen bonding environments.[28−30] Many studies have analyzed this band for bulk water as well as water in different environments.[12,31−34] Simulations of bulk water have shown the variety of hydrogen bonding environments and their relationship to the absorption spectrum and to dynamical measurements.[22,35] Addressing water dynamics and structure through experiments on the $H_2O$ hydroxyl stretch is complicated because the molecule possesses coupled symmetric and antisymmetric stretch modes that absorb in the same frequency range and overlap substantially. The bend overtone also absorbs within the OH stretch frequency range. The experiments presented below were performed on the OD stretch of dilute HOD in $H_2O$. This system simplifies the absorption spectrum because the OD stretch mode of HOD is essentially a local mode simplifying the system and making it easier to interpret the dynamics.[12] Furthermore, experiments conducted on the OD stretch of dilute HOD in $H_2O$ eliminate vibrational excitation transfer that interferes with both orientational relaxation and spectral diffusion measurements.

Below we present a comprehensive investigation exploring the effect of confinement on water dynamics in the AOT/water/isooctane reverse micelle system for a large range of sizes. Previous work using these methods exclusively targeted small reverse micelles ($w_0 = 2, 5, 10$) for the AOT/water/$CCl_4$ system,[12,14,36] demonstrating that confinement substantially affects the hydrogen bond network evolution of water. Here we examine and contrast the results of four OD hydroxyl stretch experimental observables: the IR absorption spectra, vibrational population relaxation times, orientational relaxation rates, and spectral diffusion dynamics. The measurements are conducted on samples from bulk water down to water nanopools with diameter 1.7 nm. All four observables show changes as the size of the nanopool is decreased with major deviations from bulk water occurring for $w_0 = 20$ and smaller.

The experimental results from the four observables will be analyzed in detail using a core−shell model that divides the nanoscopic water pool into two subensembles. Those water molecules that are associated with the headgroups form an outer shell, and those water molecules some distance in from the headgroups form the core. The core will be modeled by the properties of bulk water, and the shell will be modeled by the properties of the $w_0 = 2$ reverse micelle, in which essentially all waters are associated with the headgroups. It will be demonstrated that the size dependent absorption spectra and population relaxation times can be reproduced quantitatively as properly weighted combinations of the bulk water and $w_0 = 2$ spectra and vibrational lifetimes. From the results, the shell thickness is determined. However, the same model fails to reproduce either the spectral diffusion or the orientational relaxation data. It is proposed that strong dynamical coupling between the shell and the core causes the water nanopool to have distinct dynamics from the weighted sum of shell and core dynamics when hydrogen bond structural rearrangement is involved (orientational relaxation and spectral diffusion). However, the absorption spectra and population relaxation times, which significantly depend on the local structure, do reflect the weighted sum of the shell and core properties. Therefore, the separation into core and shell is appropriate for what might be termed static observables but not dynamic observables.

For the core−shell model to be successful in describing the static observables, the time scale for the core and shell populations to exchange must be longer than the time scale of the observables. Thus the exchange must occur slower than ∼10 ps, which encompasses the time scales of time dependent observables presented below. This exchange time scale is supported by simulations in various confined environments[37,38] as well as quasi-elastic neutron scattering experiments[10] that suggest translational mobility of water is severely restricted in these systems. The data and simulations suggest that dynamical exchange takes place on the time scale of tens of picoseconds or longer. Data presented in this paper also illustrate that fast (<10 ps) core−shell population exchange cannot be happening as will be discussed further below.

The paper is organized as follows. Section II describes experimental procedures. Section III presents the results of the four types of experiments. Section IV describes the methods used to analyze the results of each observable in terms of the core−shell model and presents the results of the analysis. The reasons for the successes and failures of the analysis are discussed. Section V presents some concluding comments.

## II. Experimental Procedures

Aerosol OT, isooctane (Aldrich Inc.) and water were used without further purification. A 1.0 M stock solution of AOT in isooctane was prepared. This concentration allowed for viable cell path lengths for experiments conducted on the smaller reverse micelles. Karl-Fisher titration was used to determine the residual water content in the surfactant due to its hygroscopic nature (∼0.5 water molecules per headgroup). To prepare solutions of desired $w_0$, precise volumes of water (5% HOD in $H_2O$) were added to measured quantities of the stock solution.

The size of the water nanopool is determined by the value of $w_0$. An empirical formula relating $w_0$ to the diameter of the water pool may be used for small reverse micelles. The linear relationship $d_{wp} = 0.29w_0 + 1.1$ (nm) applies to reverse micelles in the range $w_0 = 2-20$.[39] For larger reverse micelles, dynamic light scattering measurements provide the diameter of the water pool.[40] In the experiments described in this paper, the sizes ranged from 1.7 to 28 nm. The sizes of the nanopools as well as the approximate number of encapsulated water molecules are listed in Table 1. The numbers were estimated by assuming

**TABLE 1: Reverse Micelle Water Pool Sizes and Number of Water Molecules**

| reverse micelle | diameter, nm | no. of water molecules |
|---|---|---|
| $w_0 = 2$ | 1.7 | ~40 |
| $w_0 = 5$ | 2.3 | ~300 |
| $w_0 = 10$ | 4.0 | ~1000 |
| $w_0 = 20$ | 7.0 | ~5400 |
| $w_0 = 40$ | 17 | ~77000 |
| $w_0 = 60$ | 28 | ~350000 |

that the density of water is preserved within the reverse micelles indicating the level of approximation involved. All samples were housed in cells containing two $CaF_2$ windows (3 mm thick) and a Teflon spacer with a thickness adjusted to obtain optical densities in the range 0.2−0.4 for all solutions studied. All experiments described in this paper were conducted at 25°C.

The laser system employed in these experiments has been described in detail elsewhere.[12] Briefly, 800 nm pulses are generated by a home-built Ti:sapphire/regenerative amplifier system at 1 kHz. These pulses are used to pump an optical parametric amplifier (OPA) to produce ~4 $\mu$J mid-IR pulses at ~4 $\mu$m. The power spectrum of the IR pulses has a Gaussian envelope with a 230 $cm^{-1}$ bandwidth (full width at half-maximum (fwhm)). After the mid-IR pulses are generated, the experimental system is purged with dry $CO_2$ scrubbed air to remove both atmospheric water absorptions and the strong $CO_2$ absorption. To characterize the pulses in the time domain, a nonresonant third-order signal is generated that provides a three-pulse correlation from which the pulse duration is determined. Pulse chirp is determined by doing a FROG measurement.[41] Ge and $CaF_2$ flats, which have opposing effects on the second-order dispersion of the IR pulses, are placed in the beam path at Brewster's angle, and their relative amounts are adjusted to minimize the chirp. The chirp was minimized to be less than a 2 fs across the laser spectrum.

Two types of third-order measurement techniques were employed: pump−probe and stimulated vibrational echo experiments. For the pump−probe experiments, a pump pulse excites chromophores to the first vibrational excited state of the OD hydroxyl stretch of HOD in the $H_2O$ nanopools and the subsequent time evolution is measured with a variably delayed probe pulse. Because the pump and probe pulses are polarized, the decay of the anisotropy (orientational relaxation) as well as the population relaxation can be measured. In the experiments, the pump beam is polarized horizontally, and the probe is set to ~45° polarization. A polarizer in front of the monochromator is set either horizontal (∥) or vertical (⊥), to record the two components of the anisotropy. To produce directly comparable ∥ and ⊥ datasets needed to extract the decay of the anisotropy and the population, two polarizers, a half-wave plate, and a computer controlled mechanical device for interchanging the polarizers are employed. One polarizer is set ∥. The other polarizer is set ⊥ and then followed by a half wave plate that returns the beam to ∥ following the polarization analysis by the polarizer. Therefore, the light that propagates through the monochromator and measured by an MCT detector is always "∥". A small adjustment of the probe angle around the nominal 45° is made so that in the absence of the pump beam, the MCT detector measured identical intensities for the ∥ and ⊥ polarizations. Scans of the delay line alternated between ∥ and ⊥ every scan. Thus, the magnitude of the ∥ and ⊥ components have the correct relative amplitudes. The correct amplitudes are required because the decay of the anisotropy is so slow in the smaller reverse micelles that tail matching of the data cannot be used. This procedure avoids potential pitfalls in making anisotropy

measurements.[42] The pump beam is chopped and the modulated intensity of the shot-to-shot reference detector normalized probe beam is measured with a lock-in amplifier.

For the stimulated vibrational echo experiments, three variably delayed pulses are crossed in the sample, and the vibrational echo signal emerges in a unique direction. The vibrational echo pulse is dispersed in a monochromator and a particular wavelength is detected with an InSb detector. The monochromator wavelength is set at the peak of the absorption spectrum for each reverse micelle size and bulk water for a majority of the work described in this paper. Spectrally resolving the vibrational echo eliminates contributions from the 1−2 vibrational transition and permits the data to be collected at well-defined wavelengths in the 0−1 absorption spectrum.

In the three-pulse sequence, the time between pulses 1 and 2 is $\tau$, and the time between pulses 2 and 3 is $T_w$. For fixed $T_w$, $\tau$ is scanned, and a vibrational echo decay curve is recorded. This decay curve reflects the "coherence decay". Its Fourier transform is a dynamic line shape with dynamics on longer time scales eliminated. The dynamics that occur on time scales longer than a single vibrational echo decay can be measured by varying the time delay between the second and third pulses, $T_w$. An entire decay curve is measured at each $T_w$, and the full curves are used in a quantitative analysis of the data. As $T_w$ increases, a broader distribution of water structural conformations, and therefore a wider range of frequencies, is sampled through a process termed spectral diffusion. The increase in the sampled frequencies can be viewed as an increase in the dynamic line width that is buried under the absorption spectrum. As the dynamic line width increases, the vibrational echo data decay more rapidly, and the peak of the data move toward $\tau = 0$. For each water nanopool size (reverse micelle size), a set of $T_w$ dependent decay curves is recorded and analyzed using time dependent diagrammatic perturbation theory.[12,43−47] The vibrational lifetime limits the maximum time for which data can be collected. A nonresonant signal is observed for $T_w < 200$ fs. This signal, which is caused by the nonresonant polarizability of the solvent, is centered at $\tau = 0$, and interferes with data for very short $T_w$. However, because the resonant vibrational echo data are displaced from $\tau = 0$, it is possible to obtain some information even at very short $T_w$ values despite the nonresonant signal. In addition to analyzing the complete decay curves, vibrational echo peak shifts are also employed for comparisons of different reverse micelles and bulk water.[12,14] The peak shift[48] is the difference in the peak of the vibrational echo curve from $\tau = 0$ and has been shown to track the decay of the frequency-frequency correlation function (FFCF) at long times.[48] The entire vibrational echo decay curve, and therefore the peak of the curve is related to the FFCF. The magnitudes of the peak shifts in the experiments are on the order of tens of femtoseconds. Temporal drift between the first two pulses affects the peak shift values. To eliminate the effect of this drift, the two-pulse vibrational echo emitted in a distinct direction was simultaneously detected. The two-pulse echo curve involves only the first two pulses in the sequence; it is independent of $T_w$. Therefore, its position provides a method to correct for any timing drifts in the system.

In the pump−probe and vibrational echo experiments, vibrational relaxation of the excited hydroxyl stretch can cause local heating of the sample that may be observed on the time scale of 5−100's of ps. The magnitude of the temperature change is small (fraction of 1 K). The signals and local heating effects also scale equivalently with laser intensity. The time scale for the onset of these effects is long enough not to significantly impact the vibrational echo signals because a large fraction of
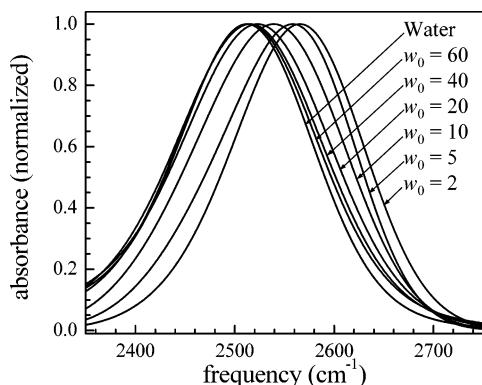
**Figure 1.** Background-subtracted FTIR absorption spectra of the OD stretch mode of 5% HOD in H₂O in bulk water and different size reverse micelles.

the dynamics occur within the first 5 ps for all samples. As a result, its effect is negligibly small for these experiments. The pump–probe experiments do measure dynamics occurring on the time scale of the local heating. The heating effects are well understood,[32,49-52] and are subtracted from the data as described in detail in the following section.

## III. Results

**A. FTIR Spectroscopy.** The linear spectroscopy of the hydroxyl stretch of water in AOT reverse micelles has been studied extensively.[12,33,34,36,53,54] Figure 1 displays the linear absorption spectra for the OD hydroxyl stretch of HOD in $H_2O$ for the bulk water and $w_0$ = 60, 40, 20, 10, 5 and 2 AOT reverse micelle samples. These spectra display an increasing blue shift as the reverse micelle size decreases. This shift has been observed by others and has been attributed to a weakening of the hydrogen bond network[33,34,53] because it is well documented that weaker hydrogen bonds absorb on the blue side of the bulk water hydroxyl stretch absorption.[35,55,56] However, attributing a blue shift of the spectrum to weaker hydrogen bonds based on the nature of bulk water can be problematic, and the interpretation of the shift will be discussed in detail below.

In contrast to the IR spectra of pure $H_2O$ in reverse micelles which contains structure in the OH stretch region,[33] the spectra of HOD in $H_2O$ exhibit no inherent structure, as can be seen in Figure 1. The bend overtone as well as symmetric and antisymmetric stretches that are coupled to the hydrogen bond network complicate the interpretation of the spectrum of pure $H_2O$ in terms of different hydrogen bonding environments. The featureless isotopically mixed absorption spectrum of the OD stretch (local mode) of HOD in reverse micelles has led to the conclusion that distinct water environments cannot be resolved by looking at the line shape of the OH or OD stretch.[53] The IR spectrum of low-frequency libration modes of water in reverse micelles suggests the possibility of two environments of water in these systems (associated and core).[57] However, the spectra are exceedingly broad, and it has been argued that the presence of an isosbestic point may not necessarily imply the existence of more than one type of chemical species in a sample.[58] There is the additional complication that the asymmetry of the absorption spectra depicted in Figure 1 may be related to a frequency dependent transition dipole of water.[59] The issue of the difference in transition dipole between bulk water and water associated with headgroups will be discussed as part of the quantitative analysis of the spectrum.

An important feature of Figure 1 is that the peak positions of the $w_0$ = 60 and 40 spectra are only slightly shifted to the

blue from the peak position of bulk water. The spectra of bulk water, $w_0$ = 60, and 40 peak at 2511, 2513, and 2516 cm⁻¹, respectively. Even though the peak shifts are small, there is noticeable broadening on the blue side of the absorption spectra. The FTIR spectra also show a distinct change in the peak position with reverse micelles $w_0$ = 20 and smaller. The $w_0$ = 20 reverse micelles correspond to a water pool diameter of ∼7 nm. Large reverse micelles contain many tens of thousands of water molecules (see Table 1), which might lead one to believe that bulk-like characteristics are to be expected. However, the broadening on the blue side of the $w_0$ = 60 and 40 spectra suggest the existence of a modified hydrogen bond network due to the presence of the interface. As shown below, all of the features in the size dependent spectra can be reproduced by the core–shell model outlined in the Introduction and applied below.

**B. Pump–Probe Spectroscopy.** The population dynamics of the OD and OH stretch have been studied extensively in different hydrogen bonded systems.[32,49-52] In all of these studies, the signals do not promptly decay to zero but persist for tens of picoseconds. The residual signals are caused by the deposition of heat following vibrational relaxation, which shifts the OD absorption spectrum.[32] These signals need to be accounted for when constructing the isotropic and anisotropic signals. This offset arises from the long-term limit of $G(t)$, a contribution to the signal that grows in as vibrational relaxation occurs. As discussed in the Experimental Section, both the parallel and perpendicular components of the pump–probe signal were measured. Measuring the signal at parallel ($S_∥$) and perpendicular ($S_⊥$) polarizations permits the determination of both the isotropic and anisotropic decays. For a dipole transition such as the OD stretch under study here,

$$S_∥(t) = P(t)[1 + 0.8C_2(t)] + G(t) \tag{2}$$

$$S_⊥(t) = P(t)[1 - 0.4C_2(t)] + G(t) \tag{3}$$

$P(t)$ represents population relaxation and $C_2(t)$ is the second Legendre polynomial correlation function describing the orientational relaxation.[60] $G(t)$ takes into account the thermal heating that results after vibrational relaxation and will be referred to as the growth term. The fact that $G(t)$ is simply added to the signals in eqs 2 and 3 assumes that the thermal heating contribution to the signal is isotropic.[32,61,62] The population relaxation is determined by constructing the isotropic signal

$$I(t) = S_∥ + 2S_⊥ = 3(P(t) + G(t)) \tag{4}$$

The growth term needs to be accounted for to obtain the vibrational population dynamics $P(t)$. In the simplest situation the population decay is a single exponential given by

$$P(t) = e^{-t/T_1} \tag{5}$$

where $T_1$ is the vibrational lifetime. $G(t)$ involves the vibrational relaxation of the hydroxyl stretch that decays to one or more intermediate states before energy finally dissipates into the ground-state bath and produces a shift of the absorption spectrum.[32] This model gives the following expression for the growth term

$$G(t) = \frac{\alpha}{k_r + k_b}[k_r(1 - \exp(-k_b t)) + k_b(-1 + \exp(-k_r t))] \tag{6}$$

$k_r = 1/T_1$ and $k_b$ is the rate constant for relaxation of intermediate

Nanoconfined Water in Reverse Micelles

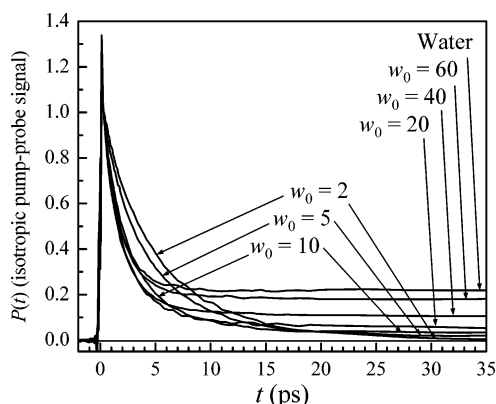*J. Phys. Chem. A, Vol. 110, No. 15, 2006* **4989**



**Figure 2.** Pump−probe data taken at the center frequency of the absorption spectrum for bulk water and different size reverse micelle samples. A nonresonant spike occurs at $t = 0$, and as a result, the data are normalized at $t = 200$ fs for comparison. The long time offsets in the data are caused by a shift in the equilibrium distribution of hydrogen bonds following vibrational relaxation (local heating).

**TABLE 2: Vibrational Lifetimes and Orientational Relaxation Parameters**

| sample | $T_1$ (ps) | $A_1$ | $\tau_1$ (ps) | $A_2$ | $\tau_2$ (ps) | $\theta_c$ | $D_c$ (ps$^{-1}$) | $D_m$ (ps$^{-1}$) |
|---|---|---|---|---|---|---|---|---|
| bulk water | 1.7 | 0.34 | 2.7 | | | | | 0.062 |
| $w_0 = 60$ | 1.8 | 0.33 | 2.7 | | | | | 0.062 |
| $w_0 = 40$ | 1.7 | 0.33 | 2.8 | | | | | 0.060 |
| $w_0 = 20$ | 2.1 | 0.33 | 3.0 | | | | | 0.056 |
| $w_0 = 10$ | 2.7 | 0.17 | 18 | 0.16 | 1.5 | 42 | 0.06 | 0.009 |
| $w_0 = 5$ | 4.4 | 0.25 | 30 | 0.08 | 1.0 | 31 | 0.05 | 0.006 |
| $w_0 = 2$ | 5.2 | 0.27 | 50 | 0.03 | 0.9 | 29 | 0.02 | 0.003 |

states leading to the spectral shift responsible for the long time offset, α.[32] To extract the rotational correlation function, the following ratio is calculated,

$$r(t) = \frac{S_\parallel - S_\perp}{S_\parallel + 2S_\perp(t) - 3G(t)} = 0.4C_2(t) \qquad (7)$$

where the denominator divides out the vibrational lifetime when the growth term is subtracted. The growth term needs to be subtracted in the denominator to give the orientational dynamics exclusively. In the absence of detectable heating induced spectral changes after vibrational relaxation (no growth term), eqs 4 and 7 yield the typical formulas that represent the isotropic and anisotropic responses.

*1. Population Relaxation.* Figure 2 presents isotropic pump−probe data obtained using the middle term of eq 4. The data curves do not decay as single exponentials. At very short time, there is a nonresonant spike that tracks the pulse duration and is negligible for the pump−probe delay time, $t > 200$ fs. The data have been normalized to 1 at $t = 200$ fs because the decays are relatively slow, the fastest being 1.7 ps (see Table 2). Two important features can be seen easily in the figure. The first feature is that the decays reflecting vibrational relaxation become increasingly fast with increasing reverse micelle size. The second feature involves the long-lived component, which increases in amplitude as the size of the water nanopool increases and attains a maximum value for bulk water.

To explore the different vibrational relaxation times, the data in Figure 2 were fit using eqs 4 and 6. As discussed in detail below, the intermediate size reverse micelles give $P(t)$'s that are not strictly single exponentials once the growth term is removed. However, initially to see the trends with nanopool size, the decays will be fit as single exponentials. The $T_1$ values

from the best single-exponential fits are given in Table 2. When bulk water is compared with water confined in a $w_0 = 2$ reverse micelle, $T_1$ increases by a factor of ∼3. $T_1$ for bulk water and $w_0 = 60$ and 40 are identical within experimental error estimated to be ±0.1 ps. By $w_0 = 20$, the lifetime has lengthened, becoming substantially longer than that of bulk water for the smaller reverse micelles. The vibrational lifetime trends we observe here are consistent with previous measurements of $T_1$ for HOD in small AOT/CCl$_4$ reverse micelles ($w_0 \leq 10$),[12] as well as measurements of $T_1$ for the OH stretch of HOD in D$_2$O.[52] Similarly, experiments probing vibrational relaxation of the azide ion in reverse micelles also show increased lifetimes for small reverse micelles.[63] The wide range of reverse micelle sizes studied here show that bulk like $T_1$ values are achieved for $w_0 > 20$ ($d_{wp} \sim 7$ nm), and that $T_1$ differs significantly for smaller reverse micelles.

The increasing long-lived component observed in the pump−probe transients can be attributed to local heating in the system. Thermally induced shifts in the absorption spectra have been observed previously for the AOT/CCl$_4$ reverse micelle system[12] as well as other hydrogen bonded systems.[50,51] The magnitude of this long-lived signal is largest for bulk water and decreases as the reverse micelle size decreases, as shown in Figure 2. In addition, the heat deposition signals decay on a shorter time scale for the smaller reverse micelles, 100 ps, increasing in time (nanoseconds) for the larger reverse micelles. The amplitude of the long-lived component with decreasing size may occur because the interface provides an avenue for some of the vibrational energy to escape the water pool during the vibrational relaxation cascade.[64]

*2. Orientational Relaxation.* The orientational dynamics were extracted from the pump−probe data using eq 7.[32,61,62] $G(t)$ is obtained from fits of the isotropic data described in the previous section. Small variations in $G(t)$ have very little effect on $r(t)$. As the nanopool size decreases, the offset also decreases, and any error introduced by the choice of $G(t)$ is further reduced. Furthermore, because the data ranges that were fit do not extend further than 35 ps, modifications to $G(t)$ involving a long time decay as heat diffuses out of the smaller reverse micelles was not introduced because the time scale associated with this (tens of picoseconds) is longer than the time range over which the data were examined. In a previous study of small AOT reverse micelles in CCl$_4$, the growth term was not included in the analysis, resulting in some errors in the values reported for the lifetimes and the orientational relaxations.[36] However, the trends presented previously are the same as those discussed below. A reanalysis of the data for the small reverse micelles studied previously[36] using the current method gave essentially identical results as those presented below for the same size micelles. Therefore, changing the solvent from CCl$_4$ to isooctane does not appear to change the dynamics of the nanoscopic water contained in the reverse micelles.

Parts A and B of Figure 3 display the anisotropy decays of bulk water and water in the different reverse micelles. There is the possibility of OD stretch excitation transfer, which would contribute to the decay of the anisotropy.[65] Faster anisotropy decays are measured for higher concentrations of HOD. Because of its strong distance dependence excitation transfer can be eliminated by lowering the concentration.[66−68] A concentration study showed evidence of excitation transfer at 10% HOD but not at 5% or 2.5%. Therefore, 5% HOD in H$_2$O samples were used in the experiments.

In all of the data it is not possible to determine the time dependence of $r(t)$ for $t < 200$ fs because of the large
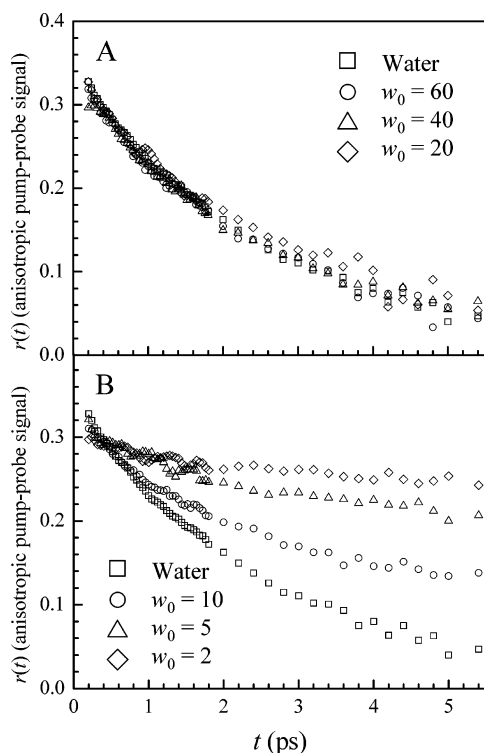
**Figure 3.** Orientational anisotropy decays of the OD stretch mode in the various samples (see Table 2). (A) Bulk water, $w_0 = 60$, 40 and 20 show little variability in the anisotropies of these samples. The decays are single exponential. (B) Bulk water, $w_0 = 10$, 5 and 2 anisotropies reveal the progressively longer orientational relaxation time scales in the smaller reverse micelles. The anisotropy decays of the small reverse micelles are biexponential.
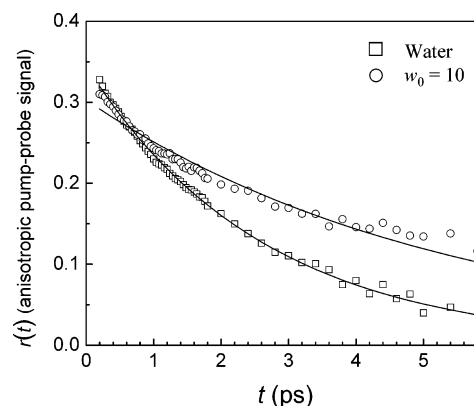


**Figure 4.** Single-exponential fits to the anisotropy decays of bulk water and the $w_0 = 10$ reverse micelle. Bulk water fits well to a single exponential whereas the $w_0 = 10$ does not.

nonresonant signal that dominates the data. Therefore, analysis of all the data begins at 200 fs. Extrapolation of the curves back to $t = 0$ never yields $r(t) = 0.4$ because there is a very fast (~50 fs) inertial component to the orientational relaxation that is complete by 200 fs.[10,37] The inertial component reduces the apparent initial anisotropy obtained by extrapolation to $t = 0$ of the measured curves.[36,62]

Figure 3A shows the data for bulk water and the three largest reverse micelles, $w_0 = 20$, 40 and 60. All of the curves are fit exceptionally well to single-exponential decays given as $\tau_1$ values in Table 2. Like the lifetime ($T_1$) results, bulk water, $w_0 = 60$ and 40, display the same orientational relaxation decay time within experimental error. The value of $\tau_1$ for $w_0 = 20$ is slightly longer and the difference from the larger reverse micelles is just outside of experimental error.

Figure 3B displays the anisotropy decays for $w_0 = 10$, 5 and 2 reverse micelles as well as bulk water. In contrast to Figure 3A, the anisotropy decays for the small reverse micelles differ substantially from bulk water. In addition, the anisotropy decays of the smaller reverse micelles are not single exponential. Figure 4, which displays anisotropy data for bulk water and $w_0 = 10$, clearly shows the difference in the functional forms of the decays. For clarity, the $w_0 = 10$ data and its single-exponential fit have been offset by +0.05 along the vertical axis. Although the water data fit very well to a single exponential, $w_0 = 10$ data are not correctly described as a single exponential. (A biexponential fit to the $w_0 = 10$ data over a much wider range of times is shown in Figure 10 and discussed below.) For the three smallest reverse micelles, Table 2 lists decay constants, $\tau_1$ and $\tau_2$ resulting from biexponential fits. The fast component, $\tau_2$, is substantially faster than bulk water and the slow component, $\tau_1$, is much slower than bulk water. Models for the

biexponential behavior will be discussed below. It is evident that a divergence of dynamical behavior occurs for water nanopool diameters of <7 nm ($w_0 = 20$). For the larger reverse micelles the anisotropy decay is single exponential and very similar to bulk water although the change may begin at $w_0 = 20$. For $w_0 \leq 10$, a ~1 ps component is followed by a component that decays in tens of picoseconds. The most dramatic affects are observed in the long time dynamics of the smallest reverse micelles. This drastic slowing down demonstrates the restrictions of structural dynamics of water molecules in small reverse micelles.

**C. Vibrational Echo Spectroscopy.** Recently, vibrational echo experiments on the hydroxyl stretch have explicated the dynamics of hydrogen bond networks in bulk water. Vibrational echo peak shift measurements[23,45] and 2D IR vibrational echo correlation spectroscopy experiments[22,44,69,70] combined with molecular dynamics simulations[35,56,59,71−76] have provided detailed information on the nature of structural evolution of bulk water's hydrogen bond network. The results demonstrate that the dynamics of water responsible for spectral diffusion observed in the experiments occur over time scales ranging from <100 fs to >1 ps. The fastest dynamics involve very local hydrogen bond fluctuations, whereas the longest time scale dynamics reflect global hydrogen bond structural rearrangement that complete the randomization of structures and the sampling of all frequencies in the hydroxyl stretch absorption spectrum.

Vibrational echo and vibrational echo peak shift measurements have been extended to small AOT reverse micelles in $CCl_4$ solvent.[12,14] Large AOT reverse micelles cannot be prepared in $CCl_4$. Preparing the reverse micelles in isooctane allowed us to revisit the small reverse micelles and extend the examination to large ones as well. Figure 5 displays time dependent vibrational echo traces for $T_w = 1.2$ ps. The water $w_0 = 60$, and 40 decays are virtually identical. The first decay that departs from bulk water behavior is for $w_0 = 20$. For water nanopools $w_0 < 20$ the differences in the decays become large. The substantial change in the nature of the dynamics at $w_0 = 20$ is consistent with the observations made of the vibrational lifetimes and orientational relaxation dynamics, where significant departure from bulk water dynamics first appear for reverse micelles smaller than $w_0 = 20$.

Data like those displayed in Figure 5 were collected for all 7 samples over a range of $T_w$ values, each $T_w$ yielding a distinct curve. The curves can be characterized by their shapes and their peak shifts, that is, the displacement of the peak of the decay curve from the absolute position of $\tau = 0$. First the data on the 7 samples will be discussed qualitatively in terms of the peak
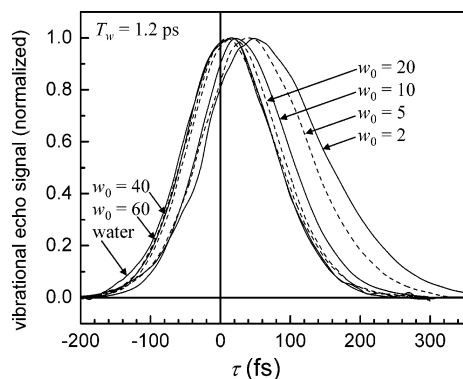
**Figure 5.** Vibrational echo decays ($\tau$ scan) at $T_w = 1.2$ ps for bulk water and different reverse micelles detected at the frequency of the center of the absorption line for each sample. Bulk water (solid line), and $w_0 = 60$, 40 and 20 (dashed lines) are not easily discernible whereas the smaller reverse micelles clearly exhibit slower decays.
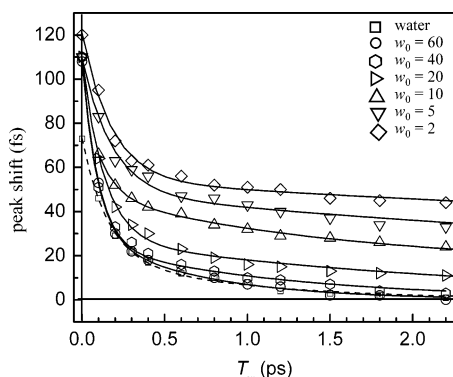


**Figure 6.** Vibrational echo peak shifts for bulk water and different reverse micelles. The lines through the data are phenomenological biexponential fits for reverse micelles (solid lines) and bulk water (dashed line). As the size of the water nanopools decrease, the spectral diffusion dynamics slow as manifested by the longer decays in the peak shifts with increasing $T_w$.

shifts. As discussed further below, the peak shifts as well as the detailed shape of the decay curves can be calculated using a model FFCF. The peak shifts provide a convenient representation of the trends in the data.

Figure 6 displays peak shift data for bulk water and the six different reverse micelles. The solid curves represent phenomenological biexponential fits rather than diagrammatic perturbation theory[43] analysis of the data,[12,14] which will be presented below. The vibrational echo peak shifts as a function of $T_w$ are related to the decay of the FFCF.[48,77] These phenomenological fits allow assessment of qualitative trends in the data prior to the detailed analysis. As structural fluctuations over a longer period of time (increased $T_w$) cause more and more of the spectroscopic line to be sampled through spectral diffusion, the peak shift goes to zero. The peak shift data at short $T_w$ (sub 500 fs) are related to the extent of the fastest structural fluctuations. As the water nanopool becomes smaller, the decay of the peak shift slows, demonstrating that the rate of structural fluctuations decrease with the nanopool size. Peak shifts for bulk water and the two largest reverse micelles, $w_0 = 60$ and 40, though quite similar, include some significant differences. Peak shifts for bulk water and $w_0 = 60$ are virtually identical after a few hundred femtoseconds. However, the initial peak shift value for water is much smaller than for $w_0 = 60$. Therefore, the very fast fluctuations in bulk water are not the same as in a water nanopool with a diameter of $\sim 28$ nm. The slower fluctuations are almost indistinguishable. Peak shifts for

**TABLE 3: FFCF Parameters**

| sample | $T_2{}^*$ (ps) | $\Delta_2$ (cm$^{-1}$) | $\tau_2$ (ps) |
|---|---|---|---|
| bulk water | 0.12 | 54 | 1.1 |
| $w_0 = 60$ | 0.12 | 57 | 1.2 |
| $w_0 = 40$ | 0.10 | 53 | 1.2 |
| $w_0 = 20$ | 0.10 | 55 | 2.5 |
| $w_0 = 10$ | 0.14 | 66 | 3.8 |
| $w_0 = 5$ | 0.16 | 54 | 6 |
| $w_0 = 2$ | 0.23 | 56 | 15 |

$w_0 = 60$ and $w_0 = 40$ are virtually identical at very short times but differ slightly at longer times. Nonetheless, except for the initial peak shift difference between bulk water and $w_0 = 60$ and $w_0 = 40$, these three samples have very similar dynamics. The significant changes in the structural fluctuations as manifested through the hydroxyl stretch frequency evolution begin at $w_0 = 20$ and become increasingly pronounced as the water nanopool size continues to decrease.

Once the FFCF has decayed significantly, further decay of the peak shift is directly related to the decay of the FFCF.[48,77] The slowest components of the phenomenological biexponential fits for the peak shifts for water, $w_0 = 60$, 40, 20, 10, 5, and 2, are approximately 1, 1, 1, 2, 4, 5, and 11 ps, respectively. These reflect the trend in the slowing of the longest component of the dynamics (complete global structural randomization of the hydrogen bond network), and in fact, are not far from the values obtained using time dependent diagrammatic perturbation theory (see Table 3).[43]

The time dependent diagrammatic perturbation theory method was used to calculate the third-order polarization generated in the sample.[43,78] The calculations employed finite pulse durations with the associated spectra. The vibrational echo curves taken at each $T_w$ and the linear line shape were fit simultaneously. The parameters used in the functional form of the FFCF were varied in fitting the data. Previous studies using 2D IR vibrational echo measurements performed with heterodyne detection (polarization level measurements) used a triexponential form for the FFCF. The full 2D correlation spectra (measured and calculated)[44,69] revealed a very fast component ($<100$ fs) that gave rise to a motionally narrowed contribution, a low amplitude intermediate component ($\sim 400$ fs), and the slowest component, 1.4 ps. The slowest component arises from global structural rearrangement of the hydrogen bond network. In the bulk water experiments, the nonresonant contribution to the signal at short time is much smaller than in the current experiments. Furthermore, the polarization level measurements afford better short time resolution compared to the intensity level measurements presented here. Given the nature of the data in the current experiments, we found a biexponential form for the FFCF was sufficient to fit the data. This reduces the number of parameters and makes comparisons between systems easier. Of particular interest here are comparisons of the longest time scale component for each system. The number obtained for bulk water is slightly faster than that obtained in the analysis of the more detailed data because the intermediate time scale component was in part subsumed into the long time scale component. However, for the purposes of understanding trends, the difference is not significant.

The functional form of the FFCF used in fitting the vibrational echo data is

$$C(t) = \Delta_1 e^{-t/\tau_1} + \Delta_2 e^{-t/\tau_2} \qquad (8)$$

where $\Delta_1$ and $\Delta_2$ are amplitude factors and $\tau_1$ and $\tau_2$ are the corresponding decay times. It is important to note that the FFCF

**4992** *J. Phys. Chem. A, Vol. 110, No. 15, 2006*

Piletic et al.

is the input into a detailed calculation of the observable. A biexponential FFCF does not produce a biexponential decay, but rather a nonexponential decay with a functional form that depends on the relative values of the parameters.

Table 3 contains the best fit parameters for all samples studied. These will be used below in the context of the core–shell model. The root-mean-squared amplitude $\Delta_1$ and time scale $\tau_1$ cannot be independently determined because the fastest time scale dephasing dynamics are motionally narrowed, that is, $\Delta_1 \tau_1 < 1$,[79,80] giving a Lorentzian contribution to the dynamic spectrum. The line width of the motionally narrowed component is $\Gamma = 1/\pi T_2^*$, with

$$1/T_2^* = \Delta_1^2 \tau_1 \qquad (9)$$

($\Delta_1$ in rad/s, $\tau_1$ in s, and $T_2^*$ in s) Although $\Delta_1$ and $\tau_1$ can be varied, they must simultaneously satisfy $\Delta_1 \tau_1 < 1$ and eq 9, which results in a well-defined value for $T_2^*$. Therefore, Table 3 lists $T_2^*$ rather than $\Delta_1$ and $\tau_1$. The $T_2^*$ values are similar until the reverse micelles become small, and then there is some increase. The $\Delta_2$ values are all very similar. The major trend with decreasing water nanopool size is a substantial increase in the long time scale time constant, $\tau_2$, for $w_0 \leq 20$. The results of these detailed fits show the same trend as the peak shift results (Figure 6), and the simple fits to the long component of the peak shifts are almost in quantitative agreement with the results given in Table 3. The change in dynamical behavior at $w_0 = 20$ is in accord with the observations of the orientational relaxation and population relaxation results.

The time dependent perturbation theory method[43] used to obtain the FFCFs involves approximations that assume the dynamics are identical across the absorption spectrum. Experiments on bulk water have shown that on short time scales (<400 fs) the rate of spectral diffusion, and therefore hydrogen bond structural dynamics, depends somewhat on wavelength because the water hydrogen bond network reflects water molecules that have different numbers and strengths of hydrogen bonds.[70] The short time scales involve very local dynamics that are sensitive to these differences. The longer time scale global hydrogen bond network rearrangements[22,44,75,76,81] involve many water molecules that are not sensitive to local details that determine the instantaneous position of a particular hydroxyl stretch in the absorption line.[70] The fact that these wavelength dependent differences are observed shows that the Gaussian approximation that underlies the diagrammatic perturbation theory determination of the FFCF is not strictly valid. Furthermore, it has been shown recently that the hydroxyl stretch transition dipole matrix element varies across the bulk water absorption line, and this variation has an impact on the vibrational echo observables.[59] For these reasons, vibrational echo data presented in Table 3 were all taken at the equivalent frequency for each sample, the peak of the absorption spectrum. Therefore, the trends observed in Table 3 will be valid although the approximations in the theory used to obtain the FFCF introduce some error.

## IV. Quantitative Test of the Core–Shell Model

Four distinct size dependent observables have been presented and discussed above. They are the IR absorption spectrum, the hydroxyl stretch population relaxation, the water orientational relaxation, and the hydroxyl stretch spectral diffusion. The discussion given above, particularly regarding small reverse micelles where deviations from bulk water are pronounced, did not directly address the issue of treating nanoscopic water as a single ensemble or as two subensembles. A single ensemble

picture does not agree with the many reports in the literature that assign distinct properties to water molecules in separate regions in the reverse micelles.[33,34,54,57,82–84] A core–shell model is based on the coexistence of a subensemble of molecules associated with the headgroups that form an outer shell of the water nanopool, and another subensemble forming the nanopool core, which has bulk water like properties ascribed to it. Though presented ubiquitously, the two subensemble model has not been rigorously tested for a variety of observables. Here each of the four observables are quantitatively tested with the two subensemble model.

**A. Spectra and Population Relaxation.** First consider the absorption spectra as a function of reverse micelle size. As shown in Figure 1, as the reverse micelle decreases in size, the spectrum shifts to the blue. One proposition to explain the shift is based on the spectrum of bulk water.[85] Water has a distribution of the number and strengths of hydrogen bonds.[21,31] On the blue side of the bulk water spectrum, water molecules with fewer and weaker hydrogen bonds comprise the spectrum; the red side reflects more and stronger hydrogen bonds. To describe the spectrum of nanoscopic water in AOT reverse micelles, a blue shift of the entire line can be attributed to a single ensemble of the water molecules having weaker and/or fewer hydrogen bonds than bulk water. As the size of the reverse micelle decreases, this picture indicates an increasing blue shift results from a decrease in the strength and/or the number of hydrogen bonds. This single ensemble description implies that the changes in the distribution of hydrogen bonding environments are continuous. This is not to say that all water molecules are alike. As in bulk water, there is a distribution of hydrogen bond strengths and number that gives rise to the broad spectroscopic line, which is inhomogeneously broadened on short time scales, as demonstrated by vibrational echo experiments.[70] However, this is a single ensemble description in the sense that it does not associate the spectroscopic changes with changes in the proportion of shell and core subensembles.

In a two subensemble model of the spectrum, overlapping contributions from a shell subensemble and a core subensemble comprise the spectrum. To test this idea, we will take the core spectrum to be the bulk water spectrum and the shell spectrum to be the $w_0 = 2$ spectrum. The $w_0 = 2$ reverse micelles have ~40 water molecules. A very simple model in which the thickness of the shell is the diameter of one water molecule, places essentially all of the $w_0 = 2$ water molecules in the shell. Figure 7A shows the bulk water and $w_0 = 2$ spectra that were used as basis spectra. All of the spectra for $w_0 = 60$ through $w_0 = 5$ were fit with the single adjustable parameter, the relative proportion of the two basis spectra. Neither the peak positions nor the widths of the basis spectra were changed in the fitting procedure. Figure 7B shows the result of this fit for $w_0 = 10$. The total $w_0 = 10$ spectrum is composed of 54% of the core (bulk water) spectrum and 46% of the shell ($w_0 = 2$) spectrum. (These are not the fractions of water molecules in the core and shell, as discussed below.) Overall, the agreement is very good with only some error in the red tail. The shape and peak position are reproduced well. Figure 7C shows the result for $w_0 = 60$. Spectra shown in Figure 1 reveal the small but noticeable differences between the bulk water spectrum and the $w_0 = 60$ spectrum; that is, the $w_0 = 60$ spectrum displays a small shift in the peak position and a broadening on the blue side of the line. The total $w_0 = 60$ spectrum is composed of 93% of the core (bulk water) spectrum and 7% of the shell ($w_0 = 2$) spectrum. These changes are reproduced quite well by the single adjustable parameter fit. The fits to all of the spectra, $w_0 = 60$
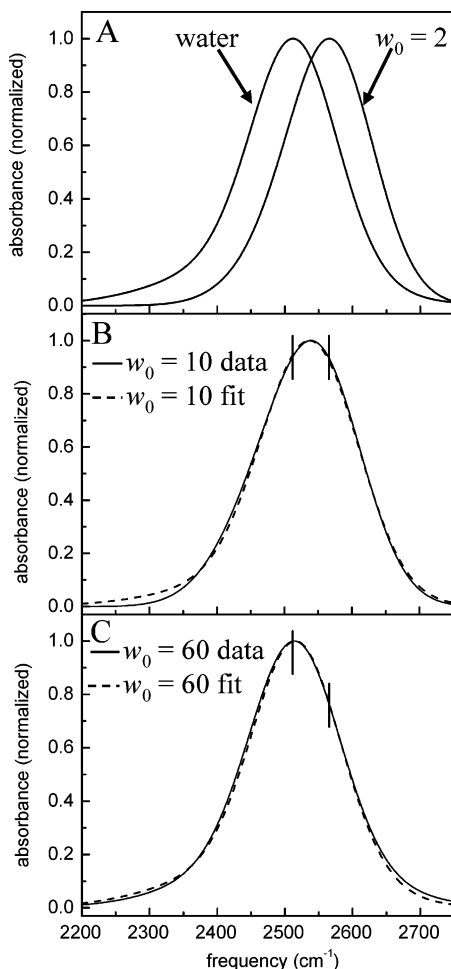
**Figure 7.** Comparison of the core−shell model to the reverse micelle size dependence of the absorption spectrum. (A) OD stretch spectra of bulk water (model of the core) and $w_0 = 2$ spectrum (model of the shell). (B) $w_0 = 10$ spectrum (solid line) and fit (dashed line). The fit is the weighted sum of the spectra in A. (C) $w_0 = 60$ spectrum and fit. The fit is the weighted sum of the spectra in (A). The small vertical lines show the peak positions of the spectra in (A).

to $w_0 = 5$, using the bulk water and the $w_0 = 2$ basis spectra gave results similar to those shown in Figure 7, although the fit for $w_0 = 5$ is not quite as good.

Not only are the changes in peak position reproduced by the core−shell model, but the changes in line widths are also reproduced. Adding an increasing amplitude of the $w_0 = 2$ spectrum (shell) to the water (core) will shift the peak to the blue and broaden the spectrum. But for the smallest reverse micelles, the spectrum narrows again as they become predominantly shell and lose amplitude on the red (core) side. In the single ensemble model of the spectrum, it is possible to explain the peak shift qualitatively as a shift of the distribution of hydrogen bonds to weaker and/or fewer, but it is less clear how to explain, even qualitatively, the broadening and then narrowing of the spectra as the size of the reverse micelles decreases. In contrast, the core−shell model reproduces that spectral feature quantitatively with a single adjustable parameter.

Next we consider the population relaxation data. A single ensemble will produce a single-exponential decay of the excited vibrational population. The results of single-exponential fits to the population data obtained after removing the growth term as discussed in connection with eq 4 are presented in Table 2 as $T_1$ values. As mentioned above, not all of the decays fit well to single exponentials. Following the very short time (∼200 fs), which is masked by the nonresonant contribution to the signal,
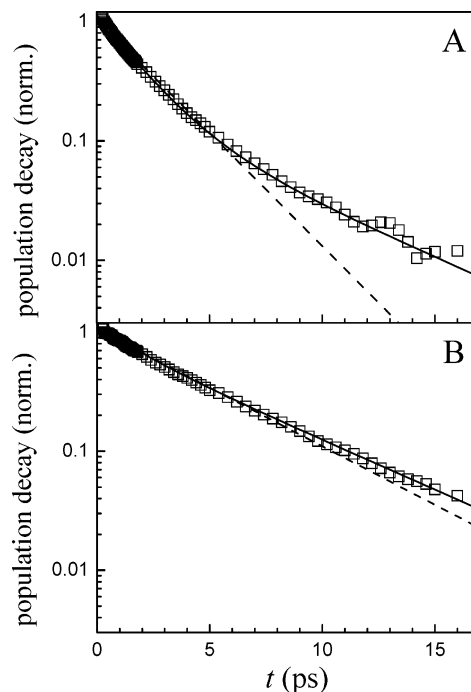


**Figure 8.** Population decay data (squares), best single-exponential fit (dashed line), and best fit with the core−shell model, that is, the weighted sum of bulk water (core model) $w_0 = 2$ (shell model) population decays: (A) $w_0 = 20$; (B) $w_0 = 5$.

bulk water and $w_0 = 2$ give single-exponential decays, within experimental error. Figure 8A shows the $w_0 = 20$ data and the best single-exponential fit (dashed line) on a semilog plot. In the fit, there are three adjustable parameters, $T_1$, $k_r$ (the rate constant in the growth term in eq 6), and an overall amplitude scaling factor. The long time limit of the growth term was fixed to the value of the data at ∼30 ps for all samples. On a longer time scale this term actually decays for the smaller reverse micelles but the dynamics at later times do not affect the data analysis presented here.[12] At short time, the single-exponential fits relatively well, but at longer times, the fit is poor. Figure 8B shows similar data for $w_0 = 5$ and the best single-exponential fit (dashed line). Again, a single exponential does a reasonable but not perfect job of reproducing the data, missing at long time. In addition to the single-ensemble model (single-exponential decay) not reproducing the data, there is no quantitative explanation for the trend of the lifetime with size, as given in Table 2.

The vibrational population relaxation data can also be analyzed quantitatively with the core−shell model. The two subensemble model can be applied by using the population dynamics measured for bulk water and $w_0 = 2$. For both of these samples, the $T_1$, and $k_r$ values are known. Therefore, rather than three parameters, these fits include only two adjustable parameters, the relative proportion of core (bulk water) and shell ($w_0 = 2$) population dynamics to be added together and an overall scaling factor. Initially, it may seem that the relative proportion should be the same as that used to fit the spectral data. However, the linear absorbance is proportional to $|\mu|^2 C$, where $\mu$ is the transition dipole bracket[86] and $C$ is the concentration, whereas the pump−probe signal is proportional to $|\mu|^4 C$ because it depends on the coupling of the oscillators to both the pump and probe pulses. The solid curves in Figure 8A,B are the best fits using the core−shell model. The results show that the two ensemble fit is substantially better with no systematic deviation between the fit and the data. The fit is better than the single-exponential fit despite the fact that there is one

fewer adjustable parameter. The $w_0 = 5$ data are closer to a single exponential than the $w_0 = 20$ data because the signal from the smaller reverse micelle is dominated by the shell contribution ($w_0 = 2$), which is single exponential. Fits to all of the different size reverse micelles, $w_0 = 60$ to 5, are of very similar quality.

For each reverse micelle size, fitting the spectra gives the relative proportion of $|\mu|^2C$ for bulk water and $w_0 = 2$, whereas fitting the population dynamics gives the relative proportion of $|\mu|^4C$. Using the two results for each reverse micelle size permits the independent determination of $|\mu|^2$ and $C$. From the results it is found that $|\mu|^2$ for bulk water is $1.4 \pm 0.2$ times larger than $|\mu|^2$ for $w_0 = 2$. This is an important result that can be independently tested by experiment. Samples of bulk water and $w_0 = 2$ (both 5% HOD) were prepared with known path lengths. The concentration of the $w_0 = 2$ sample was determined from the quantitative preparation. FT-IR spectra of the OD stretch in each sample and on the same samples but without the 5% HOD were collected. The samples without HOD were used for background subtraction. The areas of the background subtracted spectra were integrated. The ratio of the areas after taking into account the differences in path length and concentration yield the ratio of $|\mu|^2$ between the two samples. These FT-IR experiments yield a ratio of $|\mu|^2$ for bulk water to $w_0 = 2$ of $1.6 \pm 0.1$. This result provides very strong support of the core–shell model used to fit the spectra and the pump–probe population data.

With the ratio of $|\mu|^2$ determined, the ratio of $C$ for the core to shell is also determined from the spectra. The fraction of each sample that is shell for bulk water and $w_0 = 60, 40, 20, 10, 5,$ and 2, is 0.0, 0.10, 0.14, 0.26, 0.53, 0.80, and 1.0, respectively. Using the diameters of the reverse micelles given in Table 1, and a model of a spherical core surrounded by a spherical shell, the fraction that is shell for each reverse micelle can be used to determine the thickness of the shell. The shell thickness is ~0.4 nm. This value is consistent with calculations performed for similar systems.[20] As the reverse micelle increases in size, the fraction of the water molecules found in the shell region rapidly decreases. In a pump–probe experiment, the core is emphasized further by the dependence of the signal on $|\mu|^4C$. The fact that $|\mu|^2$ is ~1.6 times larger for the core than for the shell, combined with very large fraction of the water molecules in the core, accounts for the virtually identical $T_1$ values measured for bulk water, $w_0 = 60$ and 40 (Table 2).

Finally, the core–shell model for the vibrational lifetime predicts a well-defined wavelength dependence for the observed nonexponential decay. As the wavelength is shifted to the blue, more water molecules in the shell contribute, and the shape of the decay contains more amplitude of the slow component. When the wavelength is shifted to the red, more water molecules in the core contribute, although there is an additional complication because detection wavelengths on the red side of the spectra also contain contributions from the first vibrationally excited state to the second vibrationally excited-state (1–2) transition. In a preliminary study of the wavelength dependence of $w_0 = 10$, we were able to reproduce the both blue side and red side data using the core–shell model. A full wavelength study will be presented subsequently.

**B. Spectral Diffusion and Orientational Relaxation.** To further test the core–shell model, we applied it to observables that are strongly related to hydrogen bond network structural evolution. Wavelength dependent vibrational echo data were collected for $w_0 = 10$ as a good test case because our linear-IR absorption and pump–probe measurements indicate it is ap-
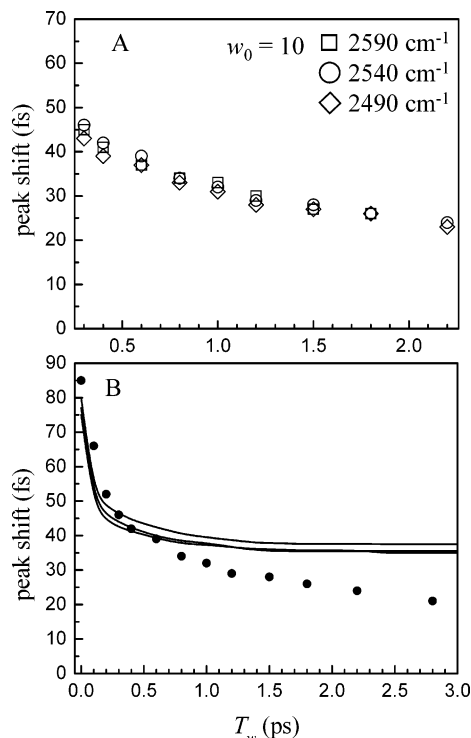


**Figure 9.** (A) Wavelength dependent vibrational echo peak shift data for $w_0 = 10$. There is no detectable wavelength dependence. (B) $w_0 = 10$ peak shift data for the center frequency (circles) and the no adjustable parameter core–shell model calculation of the three wavelengths shown in (A). In contrast to Figures 7 and 8, the core–shell model does not provide a proper description of the spectral diffusion.

proximately 47% core and 53% shell. The $w_0 = 10$ absorption spectrum peaks at ~2540 cm$^{-1}$ with a fwhm of ~175 cm$^{-1}$ (see Figures 1 and 7B). Experiments were conducted at points 50 cm$^{-1}$ to higher frequency (2590 cm$^{-1}$) and 50 cm$^{-1}$ to lower frequency (2490 cm$^{-1}$). Full vibrational echo curves were collected as a function of $T_w$. The results, shown as the $T_w$ dependent peak shifts in Figure 9A, display almost no wavelength dependence. Although these results pertain to AOT/isooctane, similar wavelength independent data were observed previously for $w_0 = 10$ in AOT/CCl$_4$.[12]

The surprising lack of wavelength dependence would seem to indicate that the two subensemble model cannot apply because signals measured at the blue and red wavelengths were expected to have substantially different contributions from the shell and core. However, in the two subensemble model, each subensemble contributes to the polarization. In the intensity level vibrational echo experiments conducted here, the signal reflects the absolute value squared of the sum of the contributions from the core and the shell subensembles. The signal is proportional to $|P_c + P_s|^2 = P_c^2 + 2P_cP_s + P_s^2$, where $P_i$ is the core and shell contributions to the total polarization. This leads to a nonnegligible cross term, $2P_cP_s$, that can produce substantial mixing and potentially reduce the wavelength dependence.

The core–shell model can be tested quantitatively for the vibrational echo observables. The FFCFs were determined for both bulk water and $w_0 = 2$ (see Table 3). Therefore, a detailed diagrammatic perturbation theory calculation can be performed for the core–shell model. For $w_0 = 10$ or any of the reverse micelles, the appropriately weighted FFCFs for the core and the shell are used in the calculation. The vibrational echo signal at the intensity level measured in these experiments is proportional to $|\mu|^8C^2$. To obtain the observables, the calculations are performed at the polarization level prior to taking the absolute

Nanoconfined Water in Reverse Micelles

*J. Phys. Chem. A, Vol. 110, No. 15, 2006* **4995**

value square of the results. The FFCF for each subensemble is weighted by the their relative values of $|\mu|^4 C$. From the experiments described in section IV.A, the relative values of $|\mu|^4 C$ are known. Therefore, the wavelength dependent vibrational echo calculations can be performed *using no adjustable parameters*.

Figure 9B displays the vibrational echo peak shift data for $w_0 = 10$ at the center frequency. Only the data set obtained at the center frequency is displayed because the data for all three wavelengths are so similar. The solid curves are the no adjustable parameter calculations for the three wavelengths displayed in Figure 9A. Several features of these data and calculations are interesting. First, like the data in Figure 9A, the calculations show little wavelength dependence, but the calculated wavelength dependence is still greater than that displayed by the data. Second, the calculated curves fundamentally have the wrong shape. Using an adjustable parameter to change the weighting of the core and shell contributions moves the calculated curves up and down but does not change their shape. At short times, the calculated curves decay too fast, and at long times, they decay far too slowly. On the time scale of the figure, the calculated curves are essentially horizontal after $\sim$2 ps.

The form of the calculated curves can be understood qualitatively. At short times, the decay is dominated by the very fast core (bulk water) decay. For $w_0 = 10$, the core would dominate the signal except for the cross term, which essentially heterodyne amplifies the shell contribution. Very qualitatively, after $\sim$2 ps the core peak shift has decayed to zero and is no longer changing. However, the shell peak shift is still significant, and it is hardly changing because its decay is very slow, $\tau_2 = 15$ ps (see Table 3). Combining a zero peak shift that is not changing with a significant peak shift that is barely changing gives a moderate peak shift that does not decay on the time scale of the plot. The vibrational echo results demonstrate that a rigid separation in core and shell subensembles does not apply, although it works very well for both the absorption spectra and the vibrational lifetimes.

The core−shell model can also be used to calculate the anisotropic pump−probe signal discussed in section III.B2. The results of the measurements are given in Table 2. The experiments illustrate that $w_0 = 10$ or smaller reverse micelles give biexponential anisotropy decays whereas the larger reverse micelles gave single-exponential decays. Like the vibrational echo calculations, the anisotropic pump−probe calculations can be done without adjustable parameters. However, to implement the core−shell model, the relations given in section III.B need to be rewritten to account for the two subensembles contributing to the signal.

The anisotropic pump−probe signal is constructed in the usual manner by combining two different measurements of the probe intensity, parallel and perpendicular, as in eq 7. As discussed in connection with eqs 4 and 6, the growth term, $G(t)$, can be removed even when two ensembles are present. However, unlike the population relaxation, $P(t)$, after eliminating $G(t)$, the resulting anisotropy equation does not necessarily isolate the orientational relaxation dynamics. To see this, eq 7 may be extended to involve two subensembles as

$$r(t) = \frac{2}{5}\left(\frac{f_C e^{-(t/T_{1C})} C_2^C(t) + f_S e^{-(t/T_{1S})} C_2^S(t)}{f_C e^{-(t/T_{1C})} + f_S e^{-(t/T_{1S})}}\right) \quad (10)$$

The prefactors $f_C$ and $f_S$ are proportional to $\mu^4 C$, which, as discussed above, are not the same for the core and the shell.
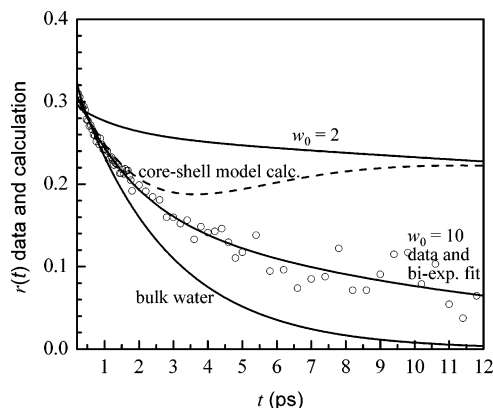


**Figure 10.** $w_0 = 10$ orientational relaxation data (circles) and biexponential fit (solid curve through circles). The upper and lower curves are the results of fits to the $w_0 = 2$ and bulk water orientational relaxation data, respectively. See Table 2 for fit parameters. The dashed curve is the core−shell model no adjustable parameter calculation of the data. See text for explanation of the shape. The core−shell model does not properly describe the orientational relaxation in reverse micelles.

This equation cannot be factored to give the pure orientational dynamics when the vibrational lifetimes and orientational correlation times of the two subensembles differ. Some interesting limits may be examined. If $T_{1C} = T_{1S}$, the anisotropy reduces to

$$r(T_w) = \frac{2}{5}\left[\left(\frac{f_C}{f_C + f_S}\right) C_2^C(t) + \left(\frac{f_S}{f_C + f_S}\right) C_2^S(t)\right] \quad (11)$$

This implies that the anisotropy will be a weighted sum of the orientational dynamics from each subensemble scaled by the transition dipoles and concentrations. If $C_2^C(t) = C_2^S(t)$, then the anisotropy reduces to

$$r(t) = \frac{2}{5} C_2(t) \quad (12)$$

which is also a result that only contains the purely orientational response. In the case of the core−shell model for AOT reverse micelles, neither of these limits are appropriate. The vibrational lifetimes and orientational correlation times are 1.7 and 2.6 ps, respectively, for bulk water and they are 5.2 and $\sim$50 ps (major component), respectively, in a $w_0 = 2$ reverse micelle. Using the core−shell model, these differing time scales produce a calculated anisotropy that does not purely reflect the orientational dynamics.

To apply the core−shell model to the anisotropy decays using eq 10 requires knowledge of all of the parameters with reasonable accuracy. Again, we use our data for $w_0 = 10$ as a test case. Figure 10 displays the measured anisotropy of the reverse micelle and the best biexponential fit (solid line) through the data. The parameters of the fit are given in Table 2. Also shown are the anisotropy decays of $w_0 = 2$ and bulk water obtained from fits to the data. The curves begin at 200 fs because the short time inertial dynamics are obscured by the nonresonant signal centered at $t = 0$.

The dashed curve shown in Figure 10 is the result of the no adjustable parameter calculation using the core−shell model given by eq 10. Initially, the match is relatively good, but at longer times the curve grows and approaches the $w_0 = 2$ curve. At still longer times, the calculated curve decays as the $w_0 = 2$ curve. The recurrence in the calculated curve does not mean that the model predicts an increase in the orientational anisot-

ropy. As can be seen from eq 10, $r(t)$ is not the anisotropy decay as it would be for a single ensemble. Rather, this curve reflects the interplay of the four terms in eq 10. To understand the shape of the curve, it is only necessary to consider the time scale of the decays of the four terms. A fast lifetime multiplied by a fast anisotropy decay comprises the first term (core term, C) in the numerator, yielding the fastest decay that looks like bulk water. The second term in the numerator (shell term, S) decays very slowly because it is a product of a slow lifetime and an even slower anisotropy decay. The second fastest term is the core term in the denominator. It is the decay of this term that is fast compared to either of the shell terms that causes the calculated curve to increase after ~3.5 ps. After the two core terms have fully decayed, the remaining shell terms in the numerator and denominator are the anisotropy decay of $w_0 = 2$. Even if the relative amounts of core and shell are adjusted, it is not possible to reproduce the data. The core−shell model of the anisotropy decay fails to fit or explain the data.

The core−shell model cannot reproduce the orientational relaxation data even qualitatively. However, a model suggested previously for orientational relaxation of small reverse micelles can produce biexponential decays for small reverse micelles[36] and provides an explanation for the transition to single-exponential decays for the larger reverse micelles. For a single ensemble of molecules undergoing unrestricted orientational diffusion $C_2(t)$ (eq 7) decays as a single-exponential decay. This model can describe the dynamics observed for water and the larger reverse micelles and yields an orientational diffusion constant[87]

$$\tau_1 = \frac{1}{6D} \tag{13}$$

The orientational dynamics of water in the smaller reverse micelles, $w_0 \leq 10$ shown in Figure 3B warrants the use of a more detailed model that can account for the restrictive orientational motions produced by the hydrogen bond network. The wobbling-in-a-cone model, which describes relaxation of a single ensemble of molecules that are orientationally restricted, can be applied. This model has been described in detail elsewhere[88] and was used to examine the orientational dynamics of water in small AOT/CCl$_4$ reverse micelles.[12] The model describes the relaxation when the orientational diffusion is restricted initially to a range of angles within a cone. In the absence of other relaxation processes, the wobbling-in-a-cone model orientational correlation function decays exponentially to a constant value. However, if there are slower time scale processes that result in complete orientational relaxation, then the wobbling-in-a-cone model yields a biexponential decay that reflects the limited diffusion within the cone as well as slower complete orientational diffusion that causes the anisotropy to decay to zero. In the standard model,[88,89] the two processes occur simultaneously. The shorter correlation time describes the restricted motion that samples a cone with semi-angle $\theta$. The longer correlation time accounts for slower unrestricted motion. The correlation function is given by

$$C_2(t) = [Q^2 + (1 - Q^2) \exp(-t/\tau_w)] \exp(-t/\tau_m) \tag{14}$$

where $Q^2$, the generalized order parameter that describes the degree of restriction on the wobbling-in-the-cone motion, is the amplitude of the slow component of the biexponential decays, and $0 \leq Q^2 \leq 1$. $Q^2 = 0$ corresponds to unrestricted reorientation, and $Q^2 = 1$ reflects no orientational relaxation. $Q^2$ is obtained from data by taking the amplitude of the slow

decay of $r(t)$ and multiplying it by 2.5 (see eq 7). $\tau_w$ is the time constant that arises from the wobbling-in-the-cone diffusion, and $\tau_m$ is the final diffusive full orientational relaxation time. For the studies reported here, $\tau_m$ is given by the long time constant $\tau_1$ in Table 2 and directly gives the orientational diffusion coefficient, $D_m$, of the angularly unrestricted orientation relaxation using eq 13. In contrast, $\tau_w$ is not directly related to experimental observables. Rather,

$$\tau_w = (\tau_2^{-1} - \tau_1^{-1})^{-1} \tag{15}$$

The cone semi-angle $\theta$ is obtained from $Q^2$ using[89]

$$Q^2 = \left[\frac{1}{2}(\cos \theta)(1 + \cos \theta)\right]^2 \tag{16}$$

If $\theta \leq 30°$, the wobbling-in-a-cone diffusion constant, $D_w$, is approximately[89]

$$D_w \cong 7\theta^2/24\tau_w \tag{17}$$

with $\theta$ in radians. From eq 17 it is clear that the wobbling diffusion constant is not determined solely by $\tau_w$. The more accurate expression for any value of $\theta_w$ leading to values reported in Table 2 is[89]

$$D_w = \frac{x_w^2(1 + x_w)^2\{\ln[(1 + x_w)/2] + (1 - x_w)/2\}}{\tau_w(1 - Q^2)[2(x_w - 1)]} + \frac{(1 - x_w)(6 + 8x_w - x_w^2 - 12x_w^3 - 7x_w^4)}{24\tau_w(1 - Q^2)} \tag{18}$$

where $x_w = \cos \theta_w$. In the limit of $\theta_w = 180°$; i.e., there is no restriction to the orientational diffusion, $Q^2 = 0$ and $D_w = 1/6\tau_w$, as expected.

Values for $\theta$, $D_w$ and $D_m$ are given in Table 2 for $w_0 = 10$, 5, and 2. Because $\tau_1$ is so much longer than $\tau_2$, $\tau_2$ and $\tau_w$ differ very little (see eq 15). These values reveal a pronounced change between $w_0 = 10$ and 20. In addition to requiring the wobbling-in-a-cone model for $w_0 = 10$ and small reverse micelles but not above $w_0 = 20$, $D_m$ drops by a factor of 6 and continues to drop with decreasing $w_0$. Furthermore, the cone angle decreases with decreasing $w_0$, indicating increasing restriction in the reverse micelle environment.

Our observation of single-exponential decay for reorientation in large reverse micelles and biexponential decay in smaller reverse micelles is consistent with the wobbling-in-a-cone model. The wobbling occurs because a restricted range of orientations is sampled on a time scale short compared to complete orientational relaxation that requires complete randomization of the hydrogen bond network (breaking and making new hydrogen bonds). If the cone angular limit is reached rapidly compared to the hydrogen bond network randomization, then a separation of time scales exists, and a biexponential decay will be observed. For $w_0 = 10$, wobbling (1.5 ps) is still fast compared to complete randomization (18 ps). By $w_0 = 20$, $\tau_1$ has dropped a factor of 6 to 3 ps, and the trend in $\tau_2$ is that it is becoming longer. There is no longer a separation of time scales. Complete randomization is occurring prior to the cone angular limit be reached and the result is a single-exponential decay. Thus, it is possible to explain the orientational relaxation data without the core−shell model, whereas the core−shell model is both quantitatively and qualitatively incorrect.

**C. Reconciling the Successes and Failures of the Strict Core−Shell Model.** In section IV.A, a core−shell model was shown to have remarkable success in reproducing the reverse

micelle size dependent trends in the absorption spectra and the population relaxation. If the reverse micelle core is modeled by bulk water data and the shell by the $w_0 = 2$ data, the appropriate addition of a core component and a shell component could reproduce all of the data with remarkable fidelity (see Figures 7 and 8). The results define a strict core–shell model in the sense that the observables are the weighted sum of the observables associated with each subensemble. However, when the identical strict core–shell model was applied in the appropriate manner to spectral diffusion and orientational relaxation in section IV.B, the calculations based on the two subensembles produced results that were fundamentally at odds with the data. The reason for success with two observables and the failure with two others lies in the differences in the nature of the properties measured in the four types of experiments.

The steady-state spectra and the population relaxation are very sensitive to the quantized energy levels of the system, whereas the hydrogen bond structural rearrangement dominates the spectral diffusion and the orientational relaxation. The absorption spectra measure the distribution of the frequencies of the OD hydroxyl stretch and report the instantaneous distribution of frequencies of the system. OD oscillators in different environments will have different stretch frequencies. Indeed, ions change both the water structure and dynamics.[3,90] It is not surprising that shell water molecules in close proximity to the charged surfactant headgroups with associated $Na^+$ counterions will have a different distribution of frequencies than those in the core, which are removed from the immediate vicinity of the headgroups.[17] Although the spectrum depends only on the frequency of the OD stretch, vibrational relaxation depends on the frequency both of the OD stretch and of other quantized modes of the system. The density of states, in part, determines the vibrational relaxation rate and is expected to differ for water in reverse micelles compared with bulk water.[91] Vibrational relaxation can be described theoretically in terms of the Fourier component of the force-force correlation function at the oscillator frequency.[92–94] However, the process is quantized. A polyatomic molecule can relax into a distribution of internal and bath modes. A variety of pathways that conserve energy can be found, but not all are equally rapid.[94] For example, the OD stretch can relax into a bend and one or more quanta of the continuum of low frequency bath modes, such as torsional modes, hydrogen bond modes, and collective coupled orientational and translational motions. Because the environment affects its frequency, the OD stretch differs in the core and shell regions. However, the environment may not affect all modes in the same way. If the bend, for example, shifts differently than the stretch, then the energy that must be transferred into the bath for vibrational relaxation to occur will be different in the core and shell regions. The result will be that different bath modes with different couplings and density of states and possibly a different number of bath modes will be required to conserve energy during the relaxation process. In addition, the bath modes themselves can be expected to be different in the core and shell regions. The relaxation pathways may differ because of the proximity of the reverse micelle headgroups. Vibrational energy can transfer to modes of the surfactant in very small reverse micelles within several ps after the vibrational excitation of the water hydroxyl stretch.[64] The net result is that, on average, the two regions produce distinct population relaxation times that are independent of each other. The fact that the population decay is composed of two distinct components is strong support for previous work[10,37,38] that suggests that the core–shell water

exchange is slow. The results presented here demonstrate that exchange must occur on a time scale >10 ps.

Spectral diffusion and orientational relaxation depend on the structural dynamics of the hydrogen bonded network rather than on the location of energy levels per se. The core and shell regions, though physically distinct, are intimately connected through the hydrogen bond network. Simulations[10,19,37] and physical considerations[14,36] show that the $Na^+$ counterions are associated with the sulfonate anionic headgroups. These structures will have very large dipoles. Although the detailed structure of water associated with the headgroup/counterion is unknown, it is safe to say that the arrangement of water molecules in a shell of waters at the interface will differ substantially from bulk water. Consider a hypothetical system possessing an infinite extent of water molecules with the structure found near the interface. Such a system will have hydrogen bond dynamics that lead to global hydrogen bond rearrangement and randomization of the network that is very different from bulk water. If this infinite extent shell structure were contacted with an infinite bulk water system, at the boundary between the two there would have to be accommodation akin to the interface of two incommensurate crystal lattices. When two incommensurate crystal lattices are joined, the boundary region structure differs from both pure crystalline materials because of accommodation.[95] However, if the two types of crystals are macroscopic in extent, some distance from the boundary, their unperturbed lattice structures will exist. In the reverse micelle, a thin shell layer meets a relatively small core region. The structures of these regions differ, but their structures and particularly their long time scale global hydrogen bond dynamics are strongly coupled. Because core waters are hydrogen bonded to shell waters, the rearrangements responsible for complete spectral diffusion and full orientational relaxation in the small reverse micelles require motions that are not independent in the two regions. Therefore, the strict core–shell model does not describe the dynamics. That is, adding the data of only the shell ($w_0 = 2$) to the data that are only the core (bulk water) does not reproduce the spectral diffusion data or the orientational relaxation data for other size reverse micelles as shown in Figures 9 and 10.

The results shown in Figures 9 and 10 demonstrate that, in contrast to the spectrum and the population relaxation, a strict core–shell model does not apply to observables that depend on global hydrogen bond rearrangements. However, differences in the hydrogen bond dynamics in the core and shell regions may still be observable. As discussed in connection with Figure 9, intensity level vibrational echo measurements of spectral diffusion will not reveal core/shell differences because of the cross term between different subensembles accounts for a large part of the observed signal. However, 2D IR vibrational echo correlation spectroscopy, which heterodyne detects the vibrational echo pulse at the polarization level eliminates the cross term.[22,44,69] This method can detect wavelength dependent differences in spectral diffusion in bulk water.[70]

Although the cross term that influences the vibrational echo measurements does not influence the orientational relaxation measurements, the core/shell model still does not adequately describe orientational observables. Molecular dynamics (MD) simulations of small AOT reverse micelles that calculate orientational relaxation show differences between associated and core water molecules.[10] Both subensembles give nonexponential decays that can be described with a wobbling-in-a-cone model that we have applied in section IV.B.[36] The simulations are consistent with the results presented here that the biexponential orientational relaxation decays cannot be assigned to two distinct

subensembles each with single-exponential orientation relaxation. The simulations also suggest that there may be two subensembles, each displaying nonexponential orientational relaxation. Preliminary wavelength dependent measurements of orientational relaxation in $w_0 = 10$ reverse micelles show changes in the orientational relaxation with wavelength which indicate that some difference in dynamics exist in different parts of the reverse micelles, but not in the manner described by the *strict* core shell model. Detailed wavelength dependent studies will be presented subsequently.

## V. Concluding Remarks

A detailed study of the nature and dynamics of water in the nanoscopically confined environment of AOT reverse micelles has been presented. Four observables were studied as a function of the water nanopool size: the hydroxyl stretch absorption spectrum, vibrational population relaxation, orientational relaxation, and spectral diffusion. All four show distinct trends with size. Figure 1 and the parameters in Tables 2 and 3 show that the major changes from bulk water behavior appear to occur when the reverse micelles become smaller than $w_0 = 20$, which corresponds to a water nanopool diameter of $<7$ Å. In the small reverse micelles, the orientational relaxation slows dramatically as does the global hydrogen bond randomization determined by measurements of spectral diffusion using vibrational echoes.

A strict core–shell model was applied to all four observables. In the model, bulk water and $w_0 = 2$ properties were used as surrogates of the core and shell (headgroup region) of the reverse micelles, respectively. It was found that the size dependent spectra and the size dependent population relaxation measured with pump–probe spectroscopy could be reproduced by the appropriately weighted sum of the core and shell surrogates. The combined fits to the spectra and population relaxation permitted the relative core–shell concentrations of water and the core–shell ratio of the water transition dipole moments to be determined. The transition dipole ratio was confirmed by independent spectroscopic measurements. The results permitted the shell thickness to be estimated at ~0.4 nm. The excellent agreement between the core–shell model and the spectra and the population relaxation data (Figures 7 and 8) lend tremendous credence to viewing the reverse micelles as being composed of distinct environments *for these observables*, which depend mainly on the immediate local structure and not on the hydrogen bond network structural evolution.

In contrast to the spectra and population relaxation, detailed calculations using the strict core–shell model could not reproduce the orientational relaxation or the spectral diffusion. These observables depend strongly on global hydrogen bond network rearrangement dynamics. It was proposed the continuous hydrogen bond network couples the core and shell regions producing network dynamics that are intimately linked in the two regions and cannot be separated into distinct independent subensembles modeled as a superposition of a core region (bulk water) and a shell region ($w_0 = 2$). There still may be differences in these regions in the dynamics. Initial wavelength dependent anisotropy experiments show changes in the orientational relaxation with the detection wavelength. Detailed wavelength dependent studies and studies of other reverse micelles are in progress. These additional experiments will clarify issues that have been brought to the fore here.

**Note Added after Print Publication.** This paper was published on the Web on March 29, 2006, and in the April 20, 2006, issue with an incorrect received date at the top of p 4985. The correct received date is February 19, 2006. The electronic version was corrected and reposted to the Web issue on August 07, 2006. An Addition and Correction appears in the August 31, 2006, issue (Vol. 110, No. 34).

## References and Notes

(1) Scatena, L. F.; Brown, M. G.; Richmond, G. L. *Science* **2001**, *292*, 908.
(2) Eisenthal, K. B. *Acc. Chem. Res.* **1993**, *26*, 636.
(3) Kropman, M. F.; Bakker, H. J. *Science* **2001**, *291*, 2118.
(4) Nandi, N.; Bhattacharyya, K.; Bagchi, B. *Chem. Rev.* **2000**, *100*, 2013
(5) Kim, J.; Schmitt, U. W.; Gruetzmacher, J. A.; Voth, G. A.; Scherer, N. F. *J. Chem. Phys.* **2002**, *116*, 737.
(6) Tassaing, T.; Danten, Y.; Besnard, M. *J. Mol. Liq.* **2002**, *101*, 149.
(7) Gorbaty, Y. E.; Bondarenko, G. V.; Kalinichev, A. G.; Okhulkov, A. V. *Mol. Phys.* **1999**, *96*, 1659.
(8) Pal, S. K. P., J.; Bagchi, B.; Zewail, A. H. *J. Phys. Chem. B* **2002**, *106*, 12376.
(9) Balasubramanian, S.; Pal, S.; Bagchi, B. *Phys. Rev. Lett.* **2002**, *89*, 115505/1.
(10) Harpham, M. R.; Ladanyi, B. M.; Levinger, N. E.; Herwig, K. W. *J. Chem. Phys.* **2004**, *121*, 7855.
(11) Willard, D. M.; Riter, R. E.; Levinger, N. E. *J. Am. Chem. Soc.* **1998**, *120*, 4151.
(12) Piletic, I. R.; Tan, H.-S.; Fayer, M. D. *J. Phys. Chem. B* **2005**, *109*, 21273.
(13) Sarkar, N.; Das, K.; Datta, A.; Das, S.; Bhattacharyya, K. *J. Phys. Chem.* **1996**, *100*, 10523.
(14) Tan, H.-S.; Piletic, I. R.; Riter, R. E.; Levinger, N. E.; Fayer, M. D. *Phys. Rev. Lett.* **2005**, *94*, 057405(4).
(15) Vajda, S.; Jimenez, R.; Rosenthal, S. J.; Fidler, V.; Fleming, G. R.; Castner, E. W. *J. Chem. Soc., Faraday Trans.* **1995**, *91*, 867.
(16) Beta, I. A.; Bohlig, H.; Hunger, B. *Phys. Chem. Chem. Phys.* **2004**, *6*, 1975.
(17) Nandi, N.; Bagchi, B. *J. Phys. Chem. B* **1997**, *101*, 10954.
(18) Faeder, J.; Ladanyi, B. M. *J. Phys. Chem. B* **2001**, *105*, 11148.
(19) Abel, S.; Sterpone, F.; Bandyopadhyay, S.; Marchi, M. *J. Phys. Chem. B* **2004**, *108*, 19458.
(20) Senapati, S.; Berkowitz, M. L. *J. Chem. Phys.* **2003**, *118*, p 1937.
(21) Stillinger, F. H. *Science* **1980**, *209*, 451.
(22) Asbury, J. B.; Steinel, T.; Stromberg, C.; Corcelli, S. A.; Lawrence, C. P.; Skinner, J. L.; Fayer, M. D. *J. Phys. Chem. A* **2004**, *108*, 1107.
(23) Fecko, C. J.; Eaves, J. D.; Loparo, J. J.; Tokmakoff, A.; Geissler, P. L. *Science* **2003**, *301*, 1698.
(24) De, T. K.; Maitra, A. *Adv. Colloid Interface Sci.* **1995**, *59*, 95.
(25) Tokmakoff, A.; Fayer, M. D. *Acc. Chem. Res.* **1995**, *28*, 437.
(26) Merchant, K. A.; Thompson, D. E.; Fayer, M. D. *Phys. Rev. Lett.* **2001**, *86*, 3899.
(27) Henri-Rousseau, O.; Blaise, P. *Adv. Chem. Phys.* **1998**, *103*, 1.
(28) Laenen, R.; Rausch, C.; Laubereau, A. *J. Phys. Chem. B* **1998**, *102*, 9304.
(29) Woutersen, S.; Emmerichs, U.; Bakker, H. J. *Science (Washington, D.C.)* **1997**, *278*, 658.
(30) Pimentel, G. C.; McClella. Al. *Annu. Rev. Phys. Chem.* **1971**, *22*, 347.
(31) Marechal, Y. *J. Chem. Phys.* **1991**, *95*, 5565.
(32) Steinel, T.; Asbury, J. B.; Fayer, M. D. *J. Phys. Chem. A* **2004**, *108*, 10957.
(33) Onori, G.; Santucci, A. *J. Phys. Chem.* **1993**, *97*, 5430.
(34) Nucci, N. V.; Vanderkooi, J. M. *J. Phys. Chem. B* **2005**, *109*, 18301.
(35) Rey, R.; Møller, K. B.; Hynes, J. T. *J. Phys. Chem. A* **2002**, *106*, 11993.
(36) Tan, H.-S.; Piletic, I. R.; Fayer, M. D. *J. Chem. Phys.* **2005**, *122*, 174501(9).
(37) Faeder, J.; Ladanyi, B. M. *J. Phys. Chem. B* **2000**, *104*, 1033.
(38) Thompson, W. H. *J. Chem. Phys.* **2004**, *120*, 8125.
(39) Kinugasa, T.; Kondo, A.; Nishimura, S.; Miyauchi, Y.; Nishii, Y.; Watanabe, K.; Takeuchi, H. *Colloids Surf. A—Physicochem. Eng. Aspects* **2002**, *204*, 193.
(40) Zulauf, M.; Eicke, H.-F. *J. Phys. Chem.* **1979**, *83*, 480.
(41) Kane, D. J.; Trebino, R. *IEEE J. Quantum Electron.* **1993**, *29*, 571.
(42) Tan, H.-S.; Piletic, I. R.; Fayer, M. D. *J. Opt. Soc. Am. B: Opt. Phys.* **2005**, *22*, 2009.
(43) Mukamel, S. *Principles of Nonlinear Optical Spectroscopy*; Oxford University Press: New York, 1995.

Nanoconfined Water in Reverse Micelles

*J. Phys. Chem. A, Vol. 110, No. 15, 2006* **4999**

(44) Asbury, J. B.; Steinel, T.; Kwak, K.; Corcelli, S.; Lawrence, C. P.; Skinner, J. L.; Fayer, M. D. *J. Chem. Phys.* **2004**, *121*, 12431.

(45) Stenger, J.; Madsen, D.; Hamm, P.; Nibbering, E. T. J.; Elsaesser, T. *J. Phys. Chem. A.* **2002**, *106*, 2341.

(46) Zanni, M. T.; Asplund, M. C.; Hochstrasser, R. M. *J. Chem. Phys.* **2001**, *114*, 4579.

(47) Merchant, K. A.; Xu, Q.-H.; Thompson, D. E.; Fayer, M. D. *J. Phys. Chem. A* **2002**, *106*, 8839.

(48) Cho, M. H.; Yu, J. Y.; Joo, T. H.; Nagasawa, Y.; Passino, S. A.; Fleming, G. R. *J. Chem. Phys.* **1996**, *100*, 11944.

(49) Woutersen, S.; Emmerichs, U.; Bakker, H. J. *J. Chem. Phys.* **1997**, *107*, 1483.

(50) Gaffney, K.; Piletic, I.; Fayer, M. D. *J. Phys. Chem. A* **2002**, *106*, 9428.

(51) Gaffney, K. J.; Davis, P. H.; Piletic, I. R.; Levinger, N. E.; Fayer, M. D. *J. Phys. Chem. A* **2002**, *106*, 12012.

(52) Dokter, A. M.; Woutersen, S.; Bakker, H. J. *Phys. Rev. Lett.* **2005**, *94*, 178301.

(53) Novaki, L. P.; El Seoud, O. A. *J. Colloid Interface Sci.* **1998**, *202*, 391.

(54) Christopher, D. J.; Yarwood, J.; Belton, P. S.; Hills, B. P. *J. Colloid Interface Sci.* **1992**, *152*, 465.

(55) Lawrence, C. P.; Skinner, J. L. *J. Chem. Phys.* **2002**, *117*, 8847.

(56) Møller, K. B.; Rey, R.; Hynes, J. T. *J. Phys. Chem. A* **2004**, *108*, 1275.

(57) Venables, D. S.; Huang, K.; Schmuttenmaer, C. A. *J. Phys. Chem. B* **2001**, *105*, 9132.

(58) Geissler, P. L. *J. Am. Chem. Soc.* **2005**, *127*, 14930.

(59) Schmidt, J. R.; Corcelli, S. A.; Skinner, J. L. *J. Chem. Phys.* **2005**, *123*, 044513.

(60) Tokmakoff, A. *J. Chem. Phys.* **1996**, *105*, 1.

(61) Loparo, J. J.; Fecko, C. J.; Eaves, J. D.; Roberts, S. T.; Tokmakoff, A. *Phys. Rev. B* **2004**, *70*, 180201.

(62) Rezus, Y. L. A.; Bakker, H. J. *J. Chem. Phys.* **2005**, *123*, 114502.

(63) Zhong, Q.; Baronavski, A. P.; Owrutsky, J. C. *J. Chem. Phys.* **2003**, *118*, 7074.

(64) Deak, J. C.; Pang, Y.; Sechler, T. D.; Wang, Z.; Dlott, D. D. *Science* **2004**, *306*, 473.

(65) Szabo, A. *J. Chem. Phys.* **1984**, *81*, 150.

(66) Forster, T. *Discuss. Faraday Soc.* **1959**, *27*, 7.

(67) Gochanour, C. R.; Andersen, H. C.; Fayer, M. D. *J. Chem. Phys.* **1979**, *70*, 4254.

(68) Gochanour, C. R.; Fayer, M. D. *J. Phys. Chem.* **1981**, *85*, 1989.

(69) Asbury, J. B.; Steinel, T.; Fayer, M. D. *J. Luminescence* **2004**, *107*, 271.

(70) Steinel, T.; Asbury, J. B.; Corcelli, S. A.; Lawrence, C. P.; Skinner, J. L.; Fayer, M. D. *Chem. Phys. Lett.* **2004**, *386*, 295.

(71) Lawrence, C. P.; Skinner, J. L. *Chem. Phys. Lett.* **2003**, *369*, 472.

(72) Piryatinski, A.; Lawrence, C. P.; Skinner, J. L. *J. Chem. Phys.* **2003**, *118*, 9672.

(73) Rey, R.; Moller, K. B.; Hynes, J. T. *Chem. Rev.* **2004**, *104*, 1915.

(74) Rey, R.; Hynes, J. T. *J. Chem. Phys.* **1996**, *104*, 2356.

(75) Corcelli, S.; Lawrence, C. P.; Skinner, J. L. *J. Chem. Phys.* **2004**, *120*, 8107.

(76) Corcelli, S.; Lawrence, C. P.; Asbury, J. B.; Steinel, T.; Fayer, M. D.; Skinner, J. L. *J. Chem. Phys.* **2004**, *121*, 8897.

(77) Joo, T. H.; Jia, Y. W.; Yu, J. Y.; Jonas, D. M.; Fleming, G. R. *J. Chem. Phys.* **1996**, *104*, 6089.

(78) Mukamel, S. *Annu. Rev. Phys. Chem.* **2000**, *51*, 691.

(79) Kubo, R. A Stochastic Theory of Line-Shape and Relaxation. In *Fluctuation, Relaxation and Resonance in Magnetic Systems*; Ter Haar, D., Ed.; Oliver and Boyd: London, 1961.

(80) Joo, T.; Albrecht, A. W. *J. Chem. Phys.* **1993**, *99*, 3244.

(81) Lawrence, C. P.; Skinner, J. L. *J. Chem. Phys.* **2003**, *118*, 264.

(82) Wong, M.; Thomas, J. K.; Nowak, T. *J. Am. Chem. Soc.* **1977**, *99*, 4730.

(83) Pileni, M. P. *J. Phys. Chem.* **1993**, *97*, 6961.

(84) Maitra, A.; Jain, K. T.; Shervani, Z. *Colloids Surf.* **1990**, *47*, 255.

(85) Bertie, J.; Lan, Z. *Appl. Spectrosc.* **1996**, *50*, 1047.

(86) Fayer, M. D. *Elements of Quantum Mechanics*; Oxford University Press: New York, 2001.

(87) Berry, R. S.; Rice, S. A.; Ross, J. *Physical Chemistry*, 2nd ed.; Oxford University Press: New York, 2000.

(88) Wang, C. C.; Pecora, R. *J. Chem. Phys.* **1980**, *72*, 5333.

(89) Lipari, G.; Szabo, A. *Biophys. J.* **1980**, *30*, 489.

(90) Kropman, M. F.; Bakker, H. J. *J. Chem. Phys.* **2001**, *115*, 8942.

(91) Boyd, J. E.; Briskman, A.; Colvin, V. L.; Mittleman, D. M. *Phys. Rev. Lett.* **2001**, *87*, 147401.

(92) Oxtoby, D. W. *Adv. Chem. Phys.* **1981**, *47*, 487.

(93) Oxtoby, D. W. *Annu. Rev. Phys. Chem.* **1981**, *32*, 77.

(94) Kenkre, V. M.; Tokmakoff, A.; Fayer, M. D. *J. Chem. Phys.* **1994**, *101*, 10618.

(95) Theodorou, G.; Rice, T. M. *Phys. Rev. B* **1978**, *18*, 2840.